High-performance extended short-wavelength infrared PBn photodetectors based on InAs/GaSb/AlSb superlattices

Junkai Jiang(蒋俊锴)[1], Faran Chang(常发冉)[1], Wenguang Zhou(周文广)[1], Nong Li(李农)[1], Weiqiang Chen(陈伟强)[1], Dongwei Jiang(蒋洞微)[1,2,3], Hongyue Hao(郝宏玥)[1,2,3], Guowei Wang(王国伟)[1,2,3,†], Donghai Wu(吴东海)[1,2,3], Yingqiang Xu(徐应强)[1,2,3], and Zhi-Chuan Niu(牛智川)[1,2,3,‡]

[1] *State Key Laboratory for Superlattices and Microstructures, Institute of Semiconductors, Chinese Academy of Sciences, Beijing* 100083, *China*
[2] *College of Materials Science and Opto-Electronic Technology, University of Chinese Academy of Sciences, Beijing* 101408, *China*
[3] *Center of Materials Science and Optoelectronics Engineering, College of Materials Science and Opto-Electronic Technology, University of Chinese Academy of Sciences, Beijing* 100049, *China*

(Received 2 November 2022; revised manuscript received 3 December 2022; accepted manuscript online 9 December 2022)

High performance short-wavelength infrared PBn photodetectors based on InAs/GaSb/AlSb superlattices on GaSb substrate have been demonstrated. At 300 K, the device exhibits a 50% cut-off wavelength of ~ 2.1 μm as predicted from the band structure calculation; the device responsivity peaks at 0.85 A/W, corresponding to a quantum efficiency (QE) of 56% for 2.0 μm-thick absorption region. The dark current density of 1.03×10^{-3} A/cm^2 is obtained under 50 mV applied bias. The device exhibits a saturated dark current shot noise limited specific detectivity (D^*) of 3.29×10^{10}cm·Hz$^{1/2}$/W (at a peak responsivity of 2.0 μm) under −50 mV applied bias.

Keywords: photodetectors, infrared, superlattices

PACS: 85.60.Gz, 87.64.km, 73.21.Cd **DOI:** 10.1088/1674-1056/acaa2e

1. Introduction

Short wavelength infrared (SWIR) band, from 1 μm to 3 μm, has broad applications in civil, military, and scientific fields, including astronomical observation, optical telecommunication, and remote sensing. Compared with thermal and visible bands, SWIR band is capable of both active and passive detections, which offers unique advantages. In addition, SWIR camera can also provide high-resolution images with a long-range distance. At present, the common SWIR detector materials on the market are mainly based on InGaAs and HgCdTe. When InGaAs is lattice matched to the InP substrate, photodetectors based on InGaAs exhibit high performance with a cutoff wavelength of ~ 1.7 μm. However, to adjust the cut-off wavelength, it must be done by adjusting the components. Mismatch-induced defects[1] rapidly reduce the device performance. Therefore, the wavelength tunability of the InGaAs material system is very limited. The wavelength tunability of HgCdTe material is good, but it is limited by the uniformity of epitaxial growth of the material and the complicated device fabrication process. In contrast, InAs/GaSb type-II superlattice (T2SL) is a developing material with intrinsic advantages such as great flexibility in bandgap engineering,[2,3] high carrier effective mass,[4] Auger recombination suppression,[5] high uniformity,[6] and low growth and manufacturing cost. These advantages make InAs/GaSb T2SL an attractive candidate for the third infrared detection and imaging over the entire infrared spectrum.[7–12] Numerous material systems provide potential for photodetectors at the same time.[13–17]

The M-structure[18] SL designed based on the 6.1 Å InAs/GaSb/AlSb material system has been shown to have a larger effective carrier mass and greater freedom in tuning the band gap. Initially, the M-structure exists in the device as a barrier region, e.g., suppressing the tunneling current in p–π–M–n, blocking the majority carriers in pMp. Recently, M-structure T2SL-based photodetectors have demonstrated promising performance in SWIR[19] and SW/MW dual bands.[20] After that, back-side illuminated focal plane arrays (FPAs) due to M-structure absorption in the GaSb etch-stop layers that have been used for e-SWIR T2SL FPAs have been studied.[21] The p–i–n structure was adopted in all three reports. In contrast, XBn structure is better to suppress dark currents. PBn is a good choice due to its very low bias dependence. In this paper, we designed photodetectors with an M-structure-based absorption region in e-SWIR regime optimized for epitaxial growth. On this basis, a PBn device with an ultra-thin top contact layer and a barrier layer was fabricated, thus suppressing the dark current of the device and improving the quantum efficiency (QE). The unipolar barrier in this work is created by PBn. The nBn[22] or pBp[23] can also create a unipolar barrier, which can successfully block the dark current associated with the depletion zone without obstructing the photocurrent in the absorption region.

†Corresponding author. E-mail: wangguowei@semi.ac.cn
‡Corresponding author. E-mail: zcniu@semi.ac.cn

© 2023 Chinese Physical Society and IOP Publishing Ltd

2. Experiment

2.1. Device design

QE and dark current are important indicators to demonstrate the optical and electrical properties of devices. To achieve high-performance device operation at room temperature, suppression of device dark current and QE enhancement are two important challenges. The device structure is shown in Fig. 1. The energy band assignments of the absorption region M-structure 6/1/4/1 monolayers (MLs) InAs/GaSb/AlSb SLs and the barrier layer H-structure 5/2 MLs $AlAs_{0.09}Sb_{0.91}$/GaSb SLs are shown in the colored rectangles. The valence band offset between $AlAs_{0.09}Sb_{0.91}$ and GaSb is small due to the common-anion rule[24,25] of band arrangement; therefore, it offers little possibility of designing valence bands. Since the valence band position of InAs is lower than that of AlSb and GaSb, the valence band position of the M-structure SL in the absorption region is lower than that of the H-structure SL in the barrier region. However, the H-structure SL is a large-bandgap (> 1 eV) material; thus, the H-structure barrier is a unipolar barrier for the PBn photodetector, which can effectively suppress the generation of recombination current. Moreover, the unintentional doping of the barrier region can also effectively block the leakage channel due to the inversion band of the surface. In order to improve the QE of the photodetector, the barrier region and the top contact layer are thinned to 150 nm and 50 nm, respectively, since photons are absorbed in these two regions and cannot form photocurrent.

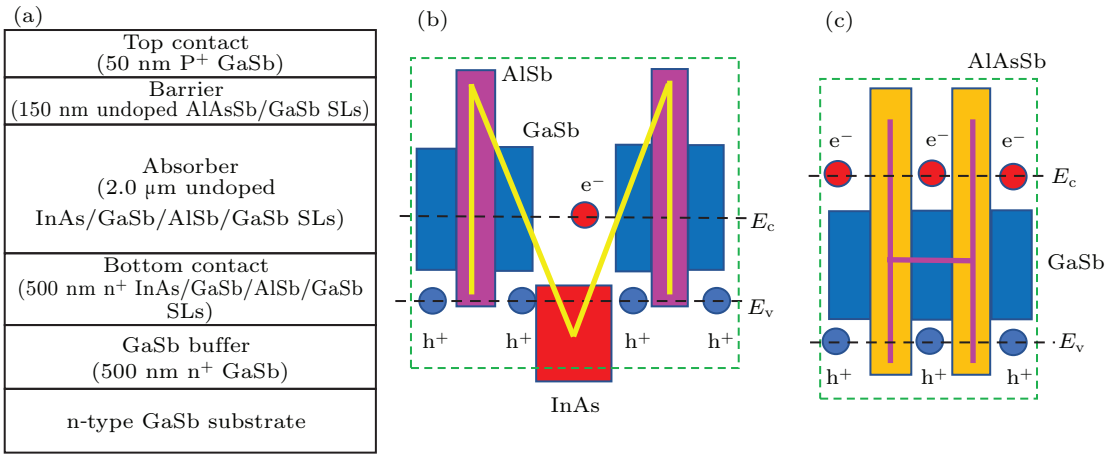


Fig. 1. (a) The schematic diagram of the InAs/GaSb/AlSb SLs PBn infrared photodetector device structure. (b) The band alignment of the M-structure 6/1/4/1 monolayers (MLs) InAs/GaSb/AlSb SLs and (c) the H-structure 5/2 MLs $AlAs_{0.09}Sb_{0.91}$/GaSb SLs for the absorption region and barrier. Colored rectangles represent the forbidden band gap of the semiconductors.

2.2. Material growth, fabrication and characterization

The material was grown on tellurium-doped n-type (001) GaSb wafer using a Veeco GEN II molecular beam epitaxy (MBE) reactor, equipped with group-III SUMO® cells and group-V valved crackers using As_2 and Sb_2. The growth was started with a 100 nm GaSb buffer layer; then, a 0.5 μm n-doped GaSb buffer layer (10^{18} cm^{-3}) which was followed by a 500 nm n-contact (10^{18} cm^{-3}), a 2 μm-thick undoped absorption region, a 150 nm barrier, and a 50 nm p-contact (10^{18} cm^{-3}). The superlattice design for bottom n-contact regions was similar to the absorption region superlattice design. The top p-contact of the original device was then replaced by a 50 nm thick, highly p-doped, GaSb capping layer. Silicon (Si) and beryllium (Be) were used as the n- and p-type dopants, respectively. Tellurium (Te) was used for the 500 nm GaSb buffer layer. In Fig. 2(d), from left to right, the band gaps are 560 meV, 560 meV, 1040 meV, and 812 meV, respectively, along the growth direction.

After the epitaxial growth, the material quality was assessed using atomic force microscopy (AFM) and high resolution x-ray diffraction (HR-XRD). The AFM showed a good surface morphology with clear atomic steps and a root mean squared (RMS) roughness of 1.78 Å over a 20×20 μm^2 area. The satellite peaks in the HR-XRD scan showed that the overall period of the as-grown superlattice was about 37 Å. The lattice mismatch between the superlattice and the GaSb substrate was less than ∼ 800 ppm.

After characterization, the superlattice wafer was processed into a set of mesa-isolated test structures with device sizes ranging from 100×100 μm^2 to 500×500 μm^2 using standard photo-lithographic processing techniques. The device mesa after inductively coupled plasma (ICP) etching is shown in Fig. 2(c). Sulfur passivation was done to suppress the dark current of the device. Then, the sample was wire-bonded to a 68-pin leadless ceramic chip carrier (LCCC). Finally, it was loaded into a cryostat for both optical and electrical characterization at temperatures ranging from 150 K to 300 K.

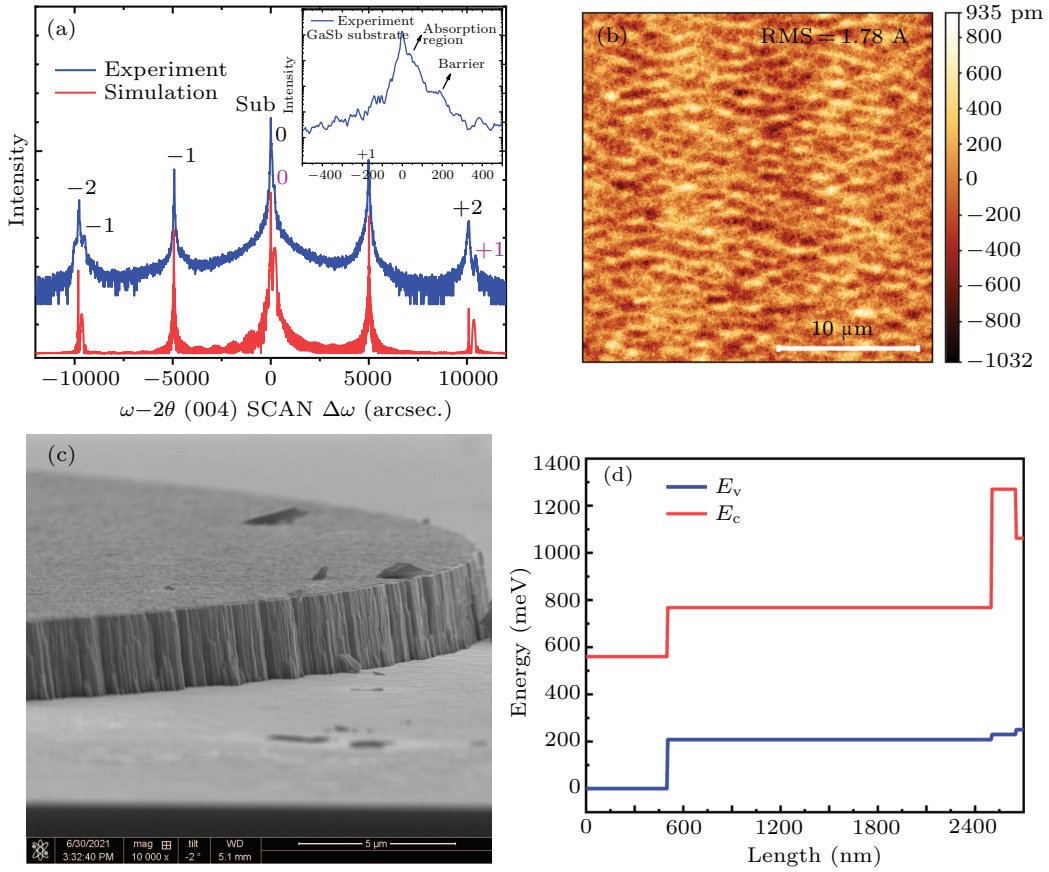


Fig. 2. (a) HR-XRD and simulation curve of the device with two series of diffraction peaks representing for the absorption region (black) and barrier (pink) based on InAs/GaSb/AlSb/GaSb SLs and AlAsSb/GaSb SLs, respectively. The inset shows the GaSb substrate and 0^{th} diffraction peaks of absorption region and barrier. (b) The atomic force microscopy image over 20 μm×20 μm surface area of the photodectector with an RMS roughness value of 1.78 Å. (c) The device mesa after ICP etching. (d) Schematic diagram of conduction (E_c) and valence (E_v) bands of the photodetector at 300 K. From left to right, the band gaps are 560 meV, 560 meV, 1040 meV, and 812 meV, respectively, along the growth direction.

3. Result and discussion

The optical characterization was done at 300 K under front-side illumination. No anti-reflection (AR) coating was applied to the photodetector. A Bruker VERTEX 70 Fourier transform infrared spectrometer (FTIR) was used to measure the photodetector spectral response. The responsivity and quantum efficiency of the photodetector were measured with a calibrated black-body source at 500 °C. The optical performance of the devices is shown in Fig. 3. The device exhibits a 50% cut-off wavelength of ∼ 2.1 μm at 300 K as predicted from the band structure calculation; the device responsivity peaks at 0.85 A/W, corresponding to a QE of 56% for the 2.0 μm-thick absorption region.

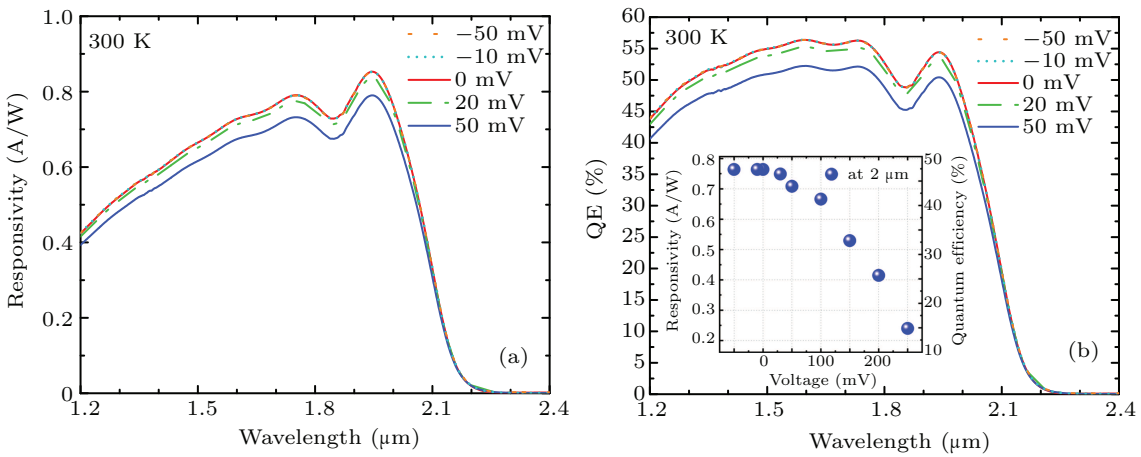


Fig. 3. (a) Responsivity spectrum and (b) quantum efficiency of the devices with a 2 μm-thick absorption region under applied bias voltage in the range from 50 mV to −50 mV in front-side illumination configuration without any anti-reflection coating. The inset shows the quantum efficiency and responsivity at 2 μm versus the applied bias.

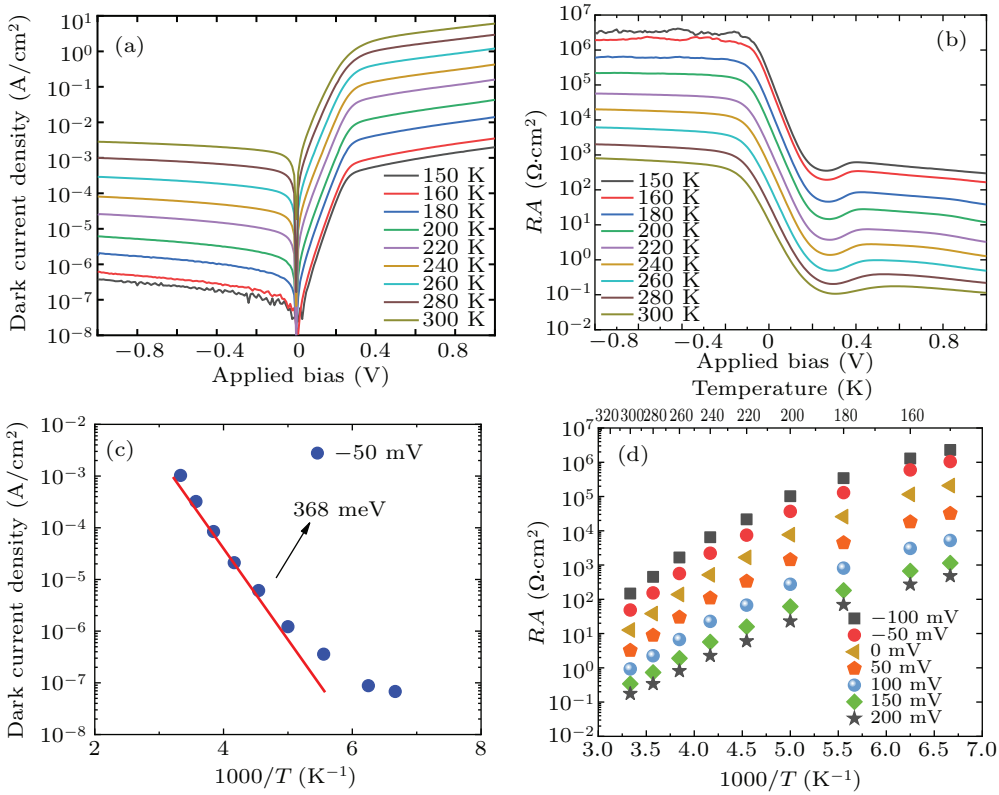


Fig. 4. (a) Dark current density vs. applied bias voltage characteristic of the photodetectors over a temperature range of 150 K to 300 K. (b) Differential resistance and area product vs. applied bias voltage characteristic of the photodetectors over a temperature range of 150 K to 300 K. (c) Arrhenius plot of the dark current of the photodetectors under −50 mV applied bias. Red lines stand for linear fit for blue point in the figure, demonstrating that 348 meV and associated activation energy (E_a) represents for the point from 220 K to 300 K. (d) Arrhenius plot of the differential resistance and area product of the photodetectors with bias voltage ranging from −100 mV to 200 mV.

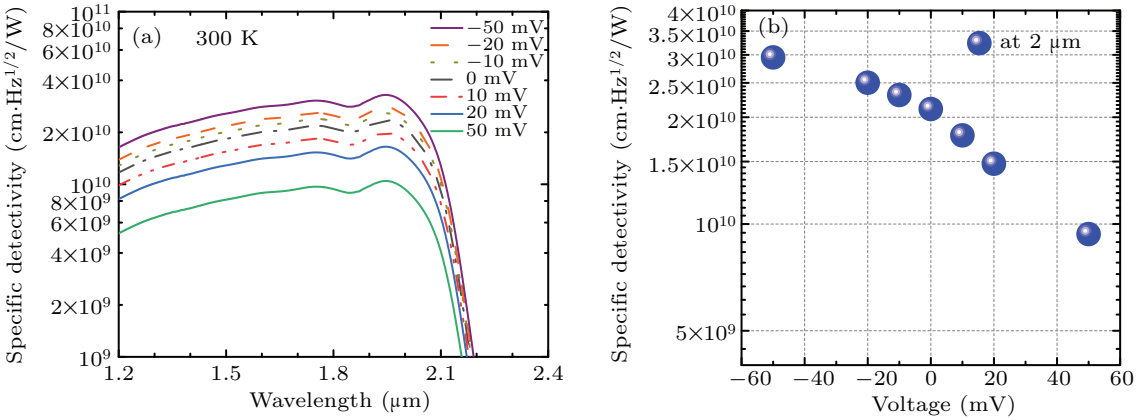


Fig. 5. (a) Specific detectivity (D^*) spectrum of the photodetector at 300 K with applied bias voltage ranging from 50 mV to −50 mV in the front illumination configuration without any anti-reflection coating. (b) The specific detectivity vs. applied bias voltage at 2 μm.

Figure 3(b) inset shows the variation of responsivity and QE with the applied voltage at 2 μm. The device responsivity and QE did not show any bias dependency; this allows for the operation of the device under small or zero bias voltages with minimal dark current. The QE of the device reaches the maximum value of 56% at 1.6 μm and remains above 50% in the 1.3–2.0 μm band. The thinning of the material thickness reduces the absorption of photons in the top contact layer and the barrier layer, further improving the quantum efficiency.[26–30] This also indicates a long diffusion length and therefore a high material quality.

The temperature dependent electrical performance was characterized with a cold shield placed in front of the photodetectors. The measured dark current density–bias voltage characteristics of the device at different temperatures are shown in Fig. 4(a). At 150 K, the dark current density of 6.80×10^{-8} A/cm^2 is obtained under 50 mV applied bias. At 300 K, the dark current density of 1.03×10^{-3} A/cm^2 is obtained under 50 mV applied bias. As shown in Fig. 4(b), the differential resistance and area product ($R\cdot A$) values of 1.04×10^{6} Ω·cm^2 and 48.6 Ω·cm^2 under −50 mV applied bias are measured at 150 K and 300 K, respectively. The varia-

tion of dark current density versus inverse temperature ($1/T$) from 150 K to 300 K is shown in Fig. 4(c). The dark current density exhibits an Arrhenius-type behavior from 220 K to 300 K with extracted associated activation energy (E_a) of about 386 meV, which is smaller than the bandgap energy of the photodetector (560 meV). It indicates that the dark current of the device is not completely dominated by the diffusion mechanism.[31–35] Therefore, it suggests that there is still room for further improvement in electrical performance of the detector by suppressing the dark current mechanisms such as generation–recombination (G-R) current.

After the electrical and optical characterization, the device specific detectivity was calculated at 300 K. The device exhibits a saturated dark current shot noise limited specific detectivity (D^*) of 3.29×10^{10} cm·Hz$^{1/2}$/W (at a peak responsivity of 2.0 μm) under −50 mV applied bias (Fig. 5(a)). As shown in Fig. 5(b), when the bias voltage of the device is less than 50 mV, the specific detectivity of the device is all above 1.00×10^{10} cm·Hz$^{1/2}$/W. The detectivities at −50 mV bias and 50 mV bias differ very little from one another. This indicates that the device is hardly influenced by the bias voltage; this allows for the operation of the device under small or zero bias voltages.

4. Conclusion

We report the design, growth, and characterization of a high-performance short-wavelength PBn photodetector based on InAs/GaSb/AlSb SLs on GaSb substrate. The AFM image shows the atomic step with a small RMS roughness value of 1.78 Å over a 20×20 μm^2 area. Satellite peaks in the HR-XRD scan show the overall periods of the absorption region in good agreement with the theoretical designs. The lattice mismatch between the absorption layer and the GaSb substrate is less than ∼ 800 ppm. At 300 K, the device exhibits a 50% cutoff wavelength of ∼ 2.1 μm as predicted from the band structure calculation; the device responsivity peaks at 0.85 A/W, corresponding to a QE of 56% for the 2.0 μm-thick absorption region. The dark current density of 1.03×10^{-3} A/cm^2 is obtained under 50 mV applied bias. The device exhibits a saturated dark current shot noise limited specific detectivity (D^*) of 3.29×10^{10} cm·Hz$^{1/2}$/W (at a peak responsivity of 2.0 μm) under −50 mV applied bias. This indicates that the device is hardly influenced by the bias voltage; this allows for the operation of the device under small or zero bias voltages.

Acknowledgements

Project supported by the National Key Technologies R&D Program of China (Grant Nos. 2019YFA0705203 and 2018YFA0209104), Major Program of the National Natural Science Foundation of China (Grant No. 61790581), and Aeronautical Science Foundation of China (Grant No. 20182436004).

References

[1] Bubulac L O, Tennant W E, Pasko J G, Kozlowski L J, Zandian M, Motamedi M E and D'souza A I 1997 *Journal of Electronic Materials* **26** 649
[2] Wei Y and Razeghi M 2004 *Phys. Rev. B* **69** 085316
[3] Piquini P, Zunger A and Magri R 2008 *Phys. Rev. B* **77** 115314
[4] Nguyen B M, Hoffman D, Delaunay P Y, Huang E K W, Razeghi M and Pellegrino J 2008 *Appl. Phys. Lett.* **93** 163502
[5] Youngdale E R, Meyer J R, Hoffman C A, *et al.* 1994 *Appl. Phys. Lett.* **64** 3160
[6] Binh-Minh N, Guanxi C, Minh-Anh H and Razeghi M 2011 *IEEE Journal of Quantum Electronics.* **47** 686
[7] Liu F, Yang S, Zhou D, *et al.* 2015 *Chin. Phys. Lett.* **32** 88503
[8] Meng W D, Zhang H F, Deng H R, *et al.* 2020 *Acta Phys. Sin.* **69** 019502 (in Chinese)
[9] Kang J B, Li Q and Li M 2019 *Acta Phys. Sin.* **68** 228501 (in Chinese)
[10] Xu B, Qiu Z Y, Yang R, *et al.* 2019 *Acta Phys. Sin.* **68** 227804 (in Chinese)
[11] Chen F Y, Lan Z, Qiang W L, *et al.* 2019 *Acta Phys. Sin.* **68** 180504 (in Chinese)
[12] Zheng W M, Huang H B, Li S M, *et al.* 2019 *Acta Phys. Sin.* **68** 187104 (in Chinese)
[13] Wang E D, Zhu B E and Gao Y 2020 *Chin. Phys. B* **29** 083101
[14] Liu Q L, Zhang H Y, Hao L X, *et al.* 2020 *Chin. Phys. B* **29** 088501
[15] Zhang M N, Shao Y, Wang X L, *et al.* 2020 *Chin. Phys. B* **29** 078503
[16] Li J S and Chen X S 2020 *Chin. Phys. B* **29** 078703
[17] Zhang M N, Shao Y, Wang X L, *et al.* 2020 *Chin. Phys. B* **29** 078503
[18] Nguyen B M, Razeghi M, Nathan V and Brown G J 2007 *Quantum Sensing and Nanophotonic Devices IV* **6479** 113
[19] Hoang AM, Chen G, Haddadi A, Abdollahi Pour S and Razeghi M 2012 *Appl. Phys. Lett.* **100** 211101
[20] Hoang A M, Chen G, Haddadi A and Razeghi M 2013 *Appl. Phys. Lett.* **102** 011108
[21] Chevallier R, Dehzangi A, Haddadii A and Razeghi M 2017 *Opt. Lett.* **42** 4299
[22] Maimon S and Wicks G W 2006 *Appl. Phys. Lett.* **89** 151109
[23] Chen Y, Wang Y, Wang Z, *et al.* 2021 *Nat. Electron.* **4** 357
[24] McCaldin J O, McGill T C and Mead C A 1976 *Phys. Rev. Lett.* **36** 56
[25] Frensley W R and Kroemer H 1977 *Phys. Rev. B* **16** 2642
[26] Jiang D W, Xiang W, Guo F Y, *et al.* 2016 *Chin. Phys. Lett.* **33** 048502
[27] Li Y, Liao S K, Liang F T, Shen Q, Liang H and Peng C Z 2016 *Chin. Phys. Lett.* **33** 030303
[28] Lv Q Q, Ye H, Yin D D, Yang X H and Han Q 2015 *Chin. Phys. Lett.* **32** 128503
[29] Ma S S, Shu T Y, Zhu J Q, *et al.* 2019 *Acta Phys. Sin.* **68** 166801 (in Chinese)
[30] Wei Z M and Xia J B 2019 *Acta Phys. Sin.* **68** 163201 (in Chinese)
[31] Liu F, Zhou D, Lu H, *et al.* 2015 *Chin. Phys. Lett.* **32** 128501
[32] Weng Q C, An Z H, Xiong D Y and Zhu Z Q 2015 *Chin. Phys. Lett.* **32** 108503
[33] Wang Y F, Qu F D, Zhou J R, *et al.* 2015 *Chin. Phys. Lett.* **32** 088504
[34] Yang G, Chen K F, Wang G, *et al.* 2020 *Chin. Phys. B* **29** 103103
[35] Wang H, Zhang Z Y, Cai X W, *et al.* 2020 *Chin. Phys. B* **29** 093601